Research Square

Preprints are preliminary reports that have not undergone peer review.
They should not be considered conclusive, used to inform clinical practice,
or referenced by the media as validated information.

Study on Leakage Detection in Earth-Rock Dams Using Airborne Infrared Thermal Imaging

Fugang Xu
Nanchang University
Kesong Zhang
Nanchang University
BoWen Wei
Nanchang University
FoLin Li
Poyang Lake Water Conservancy Hub Construction Office
Dongyang Yuan
dyyuan@ncu.edu.cn
Nanchang University
Lingyu Ouyang
Nanchang University

Research Article

Keywords: Unmanned Aerial Vehicles (UAVs), Infrared Thermography, Embankment Safety, Seepage Detection, Thermal Anomaly Identification

Posted Date: November 14th, 2026

DOI: https://doi.org/10.21203/rs.3.rs-11507602/v1

License: This work is licensed under a Creative Commons Attribution 4.0 International License.
Read Full License

Additional Declarations: No competing interests reported.

Study on Leakage Detection in Earth-Rock Dams Using Airborne Infrared Thermal Imaging

FuGang Xu,[1,2] KeSong Zhang,[1] BoWen Wei,[1] FoLin Li,[3] Dongyang Yuan,[1*] LingYu Ouyang [1]

[1]School of Infrastructure Engineering, Nanchang University, Nanchang 330031, People's Republic of China; email: Fugang Xu: xufugang092277@ncu.edu.cn, Kesong Zhang: 2711392982@qq.com, Bowen Wei: bwwei@ncu.edu.cn, Dongyang Yuan: dyyuan@ncu.edu.cn (Corresponding author), Lingyu Ouyang: ouyang_lingyu@163.com

[2]Chongqing Research Institute of Nanchang University, Chongqing 402660, People's Republic of China

[3]Poyang Lake Water Conservancy Hub Construction Office, Nanchang 330000, People's Republic of China；email: Folin Li: 3399385732@qq.com

ABSTRACT:

With the continuous increase in China's total embankment mileage, ensuring the safety and stability of these embankments has become a critical task in water conservancy engineering. Among the various hazards that threaten embankments, leakage accounts for the greatest proportion of potential risk. However, the current methods for detecting embankment leakage still rely predominantly on manual inspection methods, which are inefficient, labour-intensive, and limited in coverage. To address this technical bottleneck, this study focused on the application of airborne infrared thermal imaging technology for leakage detection in earth-rock dams. An outdoor experimental platform was constructed to fully simulate the actual operating conditions of earth-rock embankments, aiming to verify the feasibility of airborne infrared thermal imaging for detecting embankment leakage in natural environments and to clarify the laws and characteristics of thermal imaging at leakage points under different environmental conditions. The experimental results indicate that the late afternoon is the optimal time window for detecting piping hazards in earth-rock embankments using airborne infrared cameras. This is attributed to the maximum temperature difference between the piping outlet and the surrounding soil during this period, which significantly enhances the detectability of leakage signals. On thermal images, the concentrated seepage-affected area exhibits a distinctive trailing contour texture, with the temperature gradient approximately centred at the seepage outlet. Importantly, passive infrared thermal imaging can effectively detect seepage in earth-rock embankments under natural conditions, regardless of whether the downstream slope of the dam is covered with turf.and validated the feasibility of the proposed method in practical engineering cases.

PRACTICAL APPLICATIONS:

This study presents an efficient and practical solution for detecting seepage in embankments. The method employs small drones equipped with infrared cameras for inspection, eliminating the need for close manual contact and proving particularly suitable for rapid screening of large-scale, long-distance embankments. Field tests confirm optimal detection during afternoon hours when temperature differences between seepage points and surrounding soil are most pronounced, rendering them clearly distinguishable in thermal images. Regardless of whether dam slopes are grass-covered, this method effectively identifies seepage zones exhibiting “tailing” contours and temperature gradient texture patterns. This technology has been validated in real-world engineering applications, transforming traditional manual inspections into efficient aerial automated screening. It provides crucial technical support for embankment safety management.

KEYWORDS: Unmanned Aerial Vehicles (UAVs), Infrared Thermography, Embankment Safety, Seepage Detection, Thermal Anomaly Identification

1. INTRODUCTION:

As of April 2025, China has built over 98,000 reservoirs and dams, with 325,000 km of embankments rated Grade 5 or above. Earthen and rock-fill structures comprise over 85% of these (Abdelsamei et al. 2024). Increasing global climate change has raised the frequency of extreme weather such as typhoons and heavy rainfall. Combined with early construction and management limitations (Chen et al. 2022, 2024), seepage in earth-rock embankments remains serious. In the 2020 flood season alone, the middle and lower Yangtze River levees suffered over 4,300 seepage incidents, including piping and leaks. Seepage in earthen dams is highly sudden, strongly concealed, and shows subtle early signs (Duan et al. 2024; Ghimire and Schulenberg 2021), often allowing little time between onset and structural failure. Thus, rapid identification and precise localization are central to dam safety (Hu et al. 2024; Huang et al. 2022). Traditional point measurement techniques like piezometers and weirs have limited range and cannot achieve full coverage. Consequently, seepage diagnosis methods based on moisture-induced physical property differences have been developed. Geophysical techniques include transient electromagnetic (TEM) technology (Li et al. 2025; Liu et al. 2020, 2023a), which identifies water-bearing anomalies by analyzing eddy current responses to alternating magnetic fields within certain depths. Ground penetrating radar (GPR) (Liu et al. 2023b; Özer et al. 2024) uses high-frequency electromagnetic wave reflection to resolve seepage path distributions. High-density electrical methods, based on reduced resistivity in wet media, obtain 2D resistivity profiles. Distributed fibre optic temperature systems (Senarathna et al. 2024; Su et al. 2022) monitor temperature field changes to reflect seepage indirectly, offering fully distributed monitoring. However, they face bottlenecks like high cost and strict installation needs. Although better than traditional methods in scope and flexibility, significant limitations remain

(Thomas et al. 2024; Tong et al. 2024): geophysical techniques are restricted by operational conditions, limiting flood season emergency use; fibre optic monitoring still faces cost-accuracy trade-offs. Thus, there is an urgent need for leakage monitoring technology suited to large-scale, long-distance rapid inspection.

Compared to the above methods, infrared imaging offers clear advantages for identifying seepage in flood seasons. As a noncontact sensing method, airborne infrared cameras provide visual clarity, speed, mobility, and wide coverage (Wang et al. 2023a). This paper focuses on airborne infrared cameras for dam seepage detection. Recent advances in intelligent sensing and multisource data fusion are shifting seepage monitoring from manual to intelligent, 3D approaches. While manual grid-based inspection remains the foundation for flood season hazard detection, its drawbacks—low efficiency, high risk, and vulnerability to night or bad weather—are increasingly apparent. To address this, academia and industry are accelerating multimodal sensing technologies centered on infrared thermography (IRT). By analyzing the "thermal fingerprint" of seepage zones—spatiotemporal temperature variations due to water-soil heat capacity differences—a noncontact rapid diagnostic system is being built. Technically, UAV-based dual-spectrum (infrared + visible) collaborative detection has become mainstream. Systems with high-resolution infrared cameras and lidar capture both surface temperature distribution and terrain deformation along embankments, enabling real-time tracking of seepage diffusion and minute-level emergency response. To study the feasibility of detecting earthen dam seepage under natural flood conditions, a test platform simulating real flood season conditions was built. Extensive thermal imaging studies were conducted to determine optimal daily imaging windows and understand thermal characteristics of seepage outlets. Further detailed afternoon tests were performed to provide a reference for rapid airborne infrared identification of seepage in earthen dams during flood seasons.

2. METHODOLOGY:

Under the same lighting conditions, the difference in specific heat capacity between water (approximately 4.2×10^3 J/kg) and soil (approximately 0.84×10^3 J/kg) is significant. This results in different temperature change patterns for water and soil over the same lighting time. Additionally, the higher water content in areas at risk of seepage in earth–rock embankment dams leads to greater temperature changes in these areas than in nonseepage areas. The temperature change in the seepage risk area differs from that in the nonseepage areas. Currently, the use of temperature differences to identify embankment dam leakage risk has received theoretical and practical support. Unlike traditional point or line temperature measurements, infrared cameras can directly generate a two-dimensional temperature field on the surface, thus providing the basis for digital image analysis.

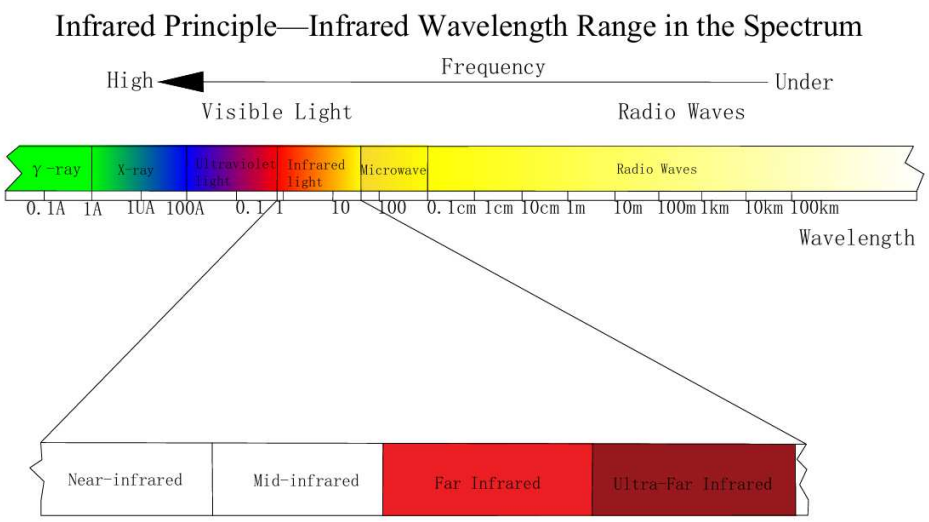


Fig. 1. Optical spectral region and energy jump correlation map

In the theory of thermal radiation, a blackbody is an idealised object that completely absorbs all incident radiation and radiates energy in the form of a continuous spectrum according to Planck's law. As shown in Fig.1.

A blackbody is considered to be a hypothetical ideal body that fully absorbs and fully radiates energy in the form of a continuous spectrum according to Planck's law, which describes the distribution of the blackbody's radiant energy at a specific wavelength and temperature:

$$M_{\lambda}(\lambda,\ T)=\frac{2\pi hc^{2}}{\lambda^{5}(\exp^{hc/kT\lambda}-1)} \quad (1)$$

where M is λ (λ, T) for the degree of outgoing radiation, that is, the unit time from the unit area of energy radiated, W/m^2; λ is the wavelength of radiation, μm; T is the thermodynamic temperature, K; h is Planck’s constant, which is 6.66 × 10-34 J - s; k is the Boltzmann constant, which is 1.3806 × 10-23 J/K; and c = 2.998 × 108 m/s, the speed of light.

The Stefan–Boltzmann law is an integral result of Planck's law, which integrates over all wavelengths to obtain the total radiated power, describes the blackbody radiation from the perspective of the overall energy, and emphasises the dominant role of temperature on the total radiated power:

$$P=\sigma T^{4} \quad (2)$$

where P is the total radiant emissivity, W/m^2; and σ = 5.67 × 10-8 W/(m2 K 4) is the Stefan–Boltzmann constant. To invert the temperature of the object by measuring the total radiant power, the emissivity ε of the object must be combined, and the correction formula is as follows:

$$P=\varepsilon\sigma T^{4} \quad (3)$$

The specific emissivity of a blackbody is 1. The emissivity of a real object $\varepsilon<1\varepsilon<1$ needs to be calibrated experimentally or by a database.

Wien's displacement law reveals a quantitative relationship between the peak wavelength of blackbody radiant energy and temperature:

$$\lambda_{\max} T = 2898 \mu\text{m} \cdot K \quad (4)$$

The peak wavelength λmax is inversely proportional to temperature; the higher the temperatu re is, the shorter the peak wavelength of the radiant energy (moving towards visible light).

Planck's law provides a microscopic description of the radiation spectrum and forms the mathematical basis for the other laws. The Stefan–Boltzmann law correlates temperature and radiation from a macroscopic, total energy perspective and guides estimates of energy intensity. Wien's displacement law optimises the selection of detection bands by identifying the peak wavelength. Together, these three laws support the design of infrared imaging systems, temperature measurement accuracy and image resolution capabilities, forming a central framework for understanding infrared physics and engineering applications. In theory, the indirect identification of earth-rock embankment leakage can be achieved by recognising image information in the thermal image.

3. EXPERIMENTAL DESIGN FOR DETECTION STUDIES:

When an infiltration gradient exists within the soil structure of an embankment and when a sudden decrease in the water level, sustained high water pressure, or external loading occurs, the fine-grained soil body migrates because of the infiltration force. As the seepage channel gradually expands, local damage is produced to the soil skeleton, resulting in the formation of a penetrating pipe surge channel. This ultimately leads to infiltration deformation evolving into overall instability. To obtain infrared image data on the apparent risk of pipe surge, analyse the infrared characteristics of the corresponding risk and provide technical support for identifying risk characteristics and reveal the mechanism of catastrophic pipe surge evolution under the influence of multiple factors, in this study, an indoor pipe surge physical simulation test system was designed and developed. According to statistics, sandy soil pipe surge is the main type of infiltration damage and triggers more than 80% of embankment failure accidents in China; thus, the test focused on the typical sand–viscous binary soil structure.

3.1 *Modelling of earth–rock dams*

The standard section of the active earth and stone embankment at Poyang Lake typically adopts a trapezoidal structure, with the embankment top generally 3–10 m higher than the inner ground. The waterside slope ratio ranges from 1:2.5 to 1:3, and the backwater side slope ratio from 1:2 to 1:2.5. This experiment aimed to identify the infrared image characteristics of seepage outlets, study the surface temperature field aberration law in seepage areas, and visualize seepage paths to reveal typical hidden

dangers in Poyang Lake embankments. Based on similarity theory, the test prioritized geometric similarity conditions and selected a model geometric scale of 1:10–1:25, covering the typical seepage scale of the thick sand layer in Poyang Lake dikes.

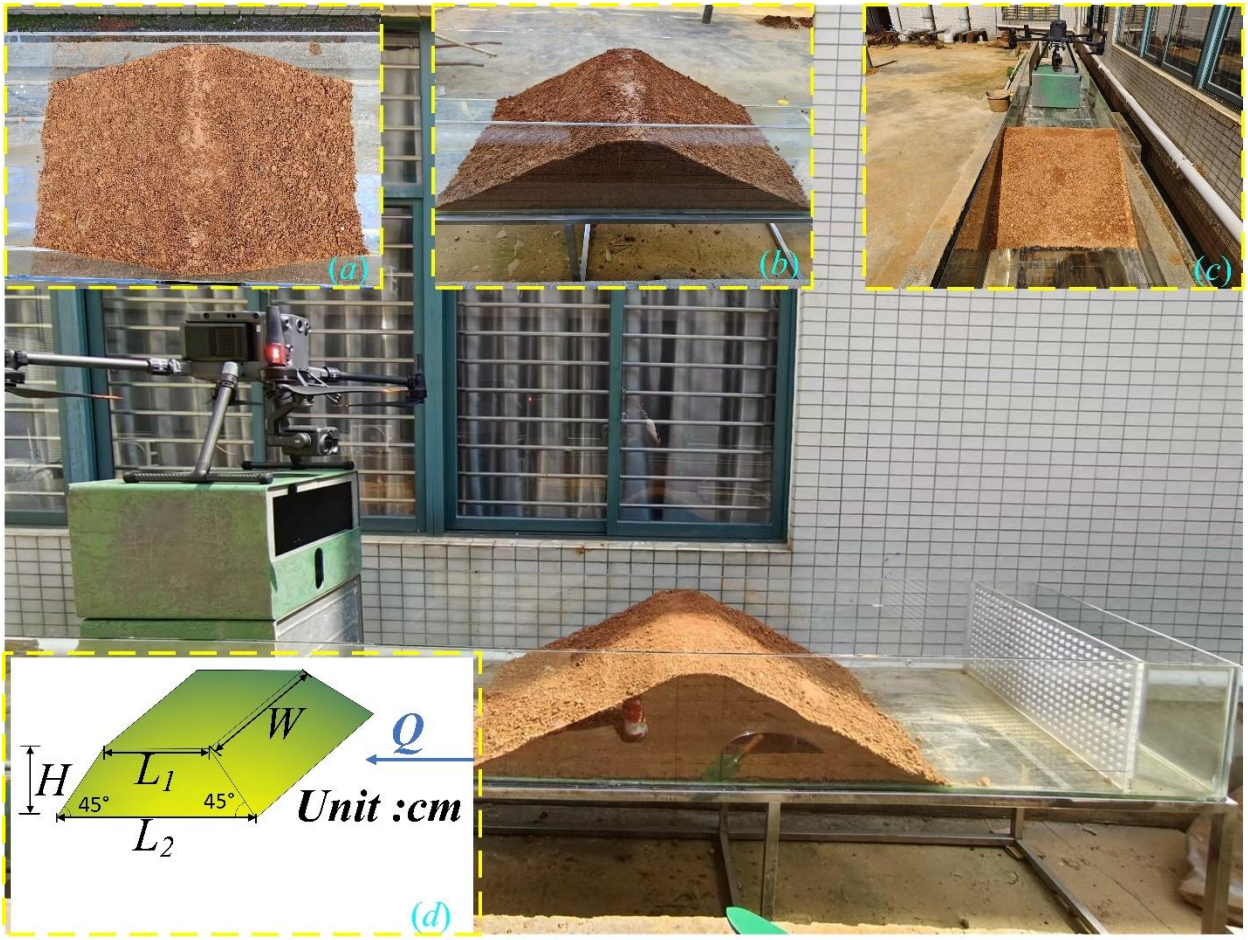


Fig.2. Arrangement of the test model platform: (*a*) top view (*b*) left view (*c*) front view (*d*) dimensions of the test dam

The experimental embankment was constructed using clayey soil, with basic physical parameters provided in Table 1. The soil dam model had the following dimensions: dam axis length of 100 cm, top width of 10 cm, maximum height of 25 cm, and both waterside and backwater side slope ratios of 1:2.5. A seepage channel was installed in the dam body, 15 cm from the left bank. To simulate the naturally formed "pipeline" resulting from soil particle loss due to water scouring in actual projects, a 1 cm diameter plastic water pipe with evenly distributed small holes was used to simulate the seepage channel, ensuring continuous seepage flow. The upstream inlet was positioned 15 cm above the riverbed, and the downstream outlet 5 cm above the riverbed, with a 1 cm thick soil cover at the outlet. The earth dam featured a secondary layered structure and was placed in an open natural environment after filling. The water level was first raised to 10 cm for 30 days to simulate normal operational conditions, then rapidly

increased to 20 cm and maintained long-term to simulate both pre-flood season prolonged immersion and flood season rapid water level rise.

Table 1 Physical Parameters of the Experimental Embankment Soil

Soil type	Plastic limit/ %	Liquid limit /%	Coefficient of permeability /(cm/s)	Dry density /(g/cm^3)
clay	15	35	1×10^{-6}~1×10^{-7}	1.6~1.8

As shown in Fig. 2, the dam body had a top width L_1 = 10 cm, length W = 100 cm, and height H = 25 cm. The experimental embankment parameters (Table 1) were based on the earth and stone embankment at Triangle Lianxu, Yongxiu County, Jiujiang City, Jiangxi Province, where both upstream and downstream slopes are 22°.

3.2 *Experimental equipment*

This paper presents an infrared thermal imaging recording carried out using a DJI Matrice 35RTK unmanned aerial vehicle (UAV) equipped with a DJI Zenmuse H20T infrared camera. On the basis of a noncontact temperature measurement module, temperature calibration was performed via multiple measurement points on the dam slope. The emissivity of the thermal imaging material was determined to be $\varepsilon = 0.96$. During testing, the vertical detection distance was maintained at 1.5 m, and the three-axis gimbal stabilisation system controlled the parallelism between the focal plane and the dam slope. The deviation of the focal plane from the dam slope was controlled to be less than 0.5°, which ensured that the imaging centre axis was aligned with the leakage-sensitive area. The results of this study confirm that the measurement error increases nonlinearly with the detection distance and that the ground resolution follows the relationship $GSD \propto d$. Moreover, deviation in the plane inclination significantly reduces the accuracy of radiometric temperature measurements. The environmental parameter monitoring used an integrated multisensor system to obtain synchronous data on water temperature, air temperature and humidity at a sampling frequency of 1 time/min, meeting the requirements for thermodynamic inversion of the seepage field of the earth dam. The technical parameters of the UAV and infrared camera are shown in Tables 2 and 3.

Table 2 Technical Parameters of the DJI Zenmuse H20T Infrared Camera

Indicator	Parameter	Unit	Indicator	Parameter	Unit
Resolution	640×512	Pixels	Working Temperature	-40~50	℃
Frame Rate	30	Hz	Temperature range	-20~1600	℃
Thermal Sensitivity	≤50	mK	Detection Distance	3~1200	m
Spatial Resolution	1.11	mrad	Data interface	SDK 3.4	—
Dust Protection	IP44	—	Storage Capacity	256	GB

Table 3 Technical Parameters of the DJI Matrice 35 RTK UAV

Indicator	Parameter	Unit	Indicator	Parameter	Unit
Dimensions	810×670×430	mm	Working Temperature	-40~50	℃
Max takeoff weight	9.2	kg	Maximum Payload	2.7	Kg
Maximum Takeoff Weight	55	min	Wind resistance	12	m/s
Maximum Horizontal Speed	23	m/s	Charging time	60	min
Dust Protection	IP44	—	Maximum Flight Altitude	5000	m

3.3 *Experimental protocol*

Levee leakage damage has significant seasonal characteristics. During the dry season, when the river's water level is low, embankment seepage damage rarely occurs. After entering the flood season, the embankment soil body experiences a complex infiltration evolution process as the water level continues to rise and remain high for a long time. The initial low water content of the upper part of the soil body is gradually saturated and softened by soaking and absorbing water over a long period. When the hydraulic gradient formed by the pore water pressure exceeds the critical seepage strength of the soil body, its structure is damaged, and internal defects continue to expand, ultimately forming seepage channels. On the basis of this seepage damage mechanism, in this study, a repeatable earth–rock embankment dam centralised seepage model test system was designed. The specific test process included four standardised phases:

(1) High-water-level infiltration simulation: Before the test started, the overflow holes and seepage channel inlets were closed, and the water level of the reservoir was increased from 10 cm to 20 cm. This simulated the continuous high water level operation conditions during the flood season, and the high water level was maintained for 60 minutes of continuous soaking. (2) Dynamic monitoring of seepage: After the infiltration process was completed, the seepage channel entrance was opened, and an infrared thermal imaging system was used to collect thermodynamic images of the seepage exit area of the backwater slope at a frequency of approximately one frame per minute. The evolution of the seepage channel morphology was recorded in real time. (3) Water level regulation and recovery: When the soil body morphology in the seepage outlet area stabilised, data acquisition was terminated. The overflow holes were opened to regulate the water level and restore the water level behind the dam to the initial low-water state. (4) Model repair and reset: Any deformed or damaged soil was removed from the dam and the same soil material as that used in the original construction of the dam was used for backfill repair. This ensured that the model geometry and material properties met the requirements for repeated testing.

4. EXPERIMENTAL RESULTS AND ANALYSIS:

4.1 *Difference in temperature patterns between river water and embankment surfaces under different environmental conditions*

The monitoring process for the surface temperature of the river water and the dam under the influence of environmental factors is shown in Fig. 3. As shown in the figure3, when daylight is present, the air and water temperatures exhibit a similar pattern of regular changes.

Typically, the air temperature increases slowly from approximately 6:00 a.m., reaches its maximum value at approximately 14:00, and then decreases until it increases again at approximately 6:00 a.m. the following day. The slope temperature changes in a similar way to the air temperature but with a slight lag. The daily maximum value is greater than the air temperature because the soil has a lower specific heat capacity than water does. Therefore, the water temperature changes with a smaller amplitude and rate than the soil and air temperature changes do, but the trends are similar. The trends of the changes in air humidity and air temperature are almost exactly the opposite. Because the specific heat capacity of water is greater than that of soil and the temperature change amplitude and rate of water are significantly lower than those of air and soil, there is an extreme difference in temperature between soil and water during the middle of the day. This time period generally occurs between 12:00 and 14:00. Considering only the temperature difference, it can be deduced that noon is the best time to detect leakage in soil and rock embankment dams when an airborne infrared camera is used. As shown in Fig. 3, humidity appeared to be negatively correlated with temperature. The red box in Fig. 3 corresponds to intermittent rainfall; persistent rainfall began on 30 May 2024 and affected both the air and slope temperatures, indicating that they are sensitive to rainfall. Rainfall has a greater effect on the difference in temperature between water and dam temperatures, and after rainfall, the dam temperature increases faster than the water temperature does. Therefore, excellent conditions may exist for detecting the leakage of earth and stone embankment dams using an airborne infrared camera after rainfall or during the middle of a sunny day.

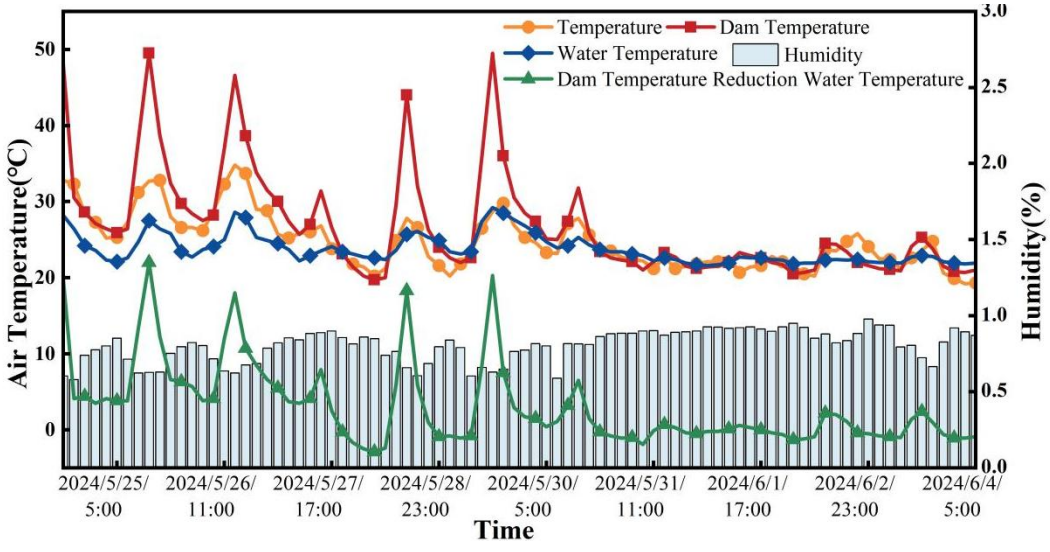


Fig.3. Time-varying process lines of environmental quantities in the test site area

4.2 *Infrared image features and patterns of seepage in uncovered slopes*

To reveal the thermal imaging characteristics of seepage outlets and their evolution, this study was based on temporal variations in environmental parameters. A systematic experimental study was carried out during midday hours (12:00–14:00), with a focus on observing the infrared response characteristics of the seepage process under different environmental conditions after rainfall had ceased and after the weather had cleared.

4.3 *Spatial distribution characteristics of thermal images of uncovered seepage outlets*

The thermal imaging and extraction results recorded during the midafternoon test are shown in Fig. 4(a and b), respectively. As with the ambient volume monitoring results, the water temperature was lower than the slope temperature during the midday hours. Low-temperature anomalies were exhibited near the seepage opening, whereas the temperature distribution in other areas was relatively uniform. This highlights the anomalies at the seepage opening. The anomalous area roughly took the opening of the pipe surge as the starting point and showed downwards gradient diffusion, resulting in the formation of a more obvious trailing tail. This feature may be important for identifying embankment seepage using infrared imaging.

In this paper, the p-quantile method was used to extract binarized segmentation results from thermal images. Unlike traditional mean reversion, the p-quantile method does not require data to follow a normal distribution or be homoskedastic, and it is more adaptable to data with heavy tails, skewness or heteroskedasticity. Calculating quartiles requires only sorting and linear interpolation, which has low computational complexity and is therefore suitable for big data scenarios. The thresholds generated by the p-quartile method are unique, making it easy for field operators to make quick judgements and reducing human error. This improves the efficiency with which danger points can be identified during the flood season.

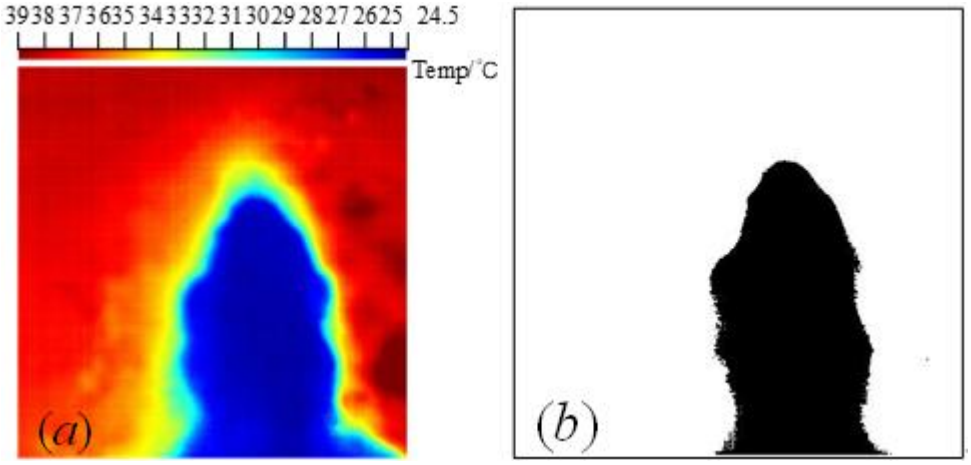


Fig. 4. Thermal images of leakage outlets and their binarized segmentation results(*a*)Leakage thermal i

mage(*b*)Leakage extraction results

4.4 *Temporal variation patterns of thermal images of seepage in uncovered slopes*

The results of the test conducted at midday on 21 June 2024 are shown in Fig. 5. It had been sunny for a week prior to the test, during which time the embankment remained at the reference level. The dam surface was wet on the inside and dry on the outside when the test was conducted. During the test, the weather was sunny with a force of 1 breeze. These weather and dam surface conditions were similar to those experienced during actual project leakage during the flood season. The embankment temperature was relatively average in all areas except at the seepage opening, where a low-temperature anomaly was observed. The water level was rapidly increased to flood the seepage inlet, indicating that this point was the starting point, i.e., t=0.

After approximately 10 minutes, temperature anomalies were observed at the leakage inlet, although no anomalies were visible in the visible light spectrum. At 18 minutes, the leakage inlet began to seep water but did not break through the surface of the embankment. The temperature anomalies spread. At 25 minutes, the leakage inlet broke through, and runoff could clearly be seen on the slope surface. The temperature anomalies spread to both sides of the trend. The trailing end of the low-temperature anomaly zone in the thermal image gradually expanded over time. After approximately 45 minutes, the low-temperature anomalous area ultimately formed a more stable trailing pattern.

The results of the test conducted at midday on 26 June 2024 are shown in Fig. 6. Following the previous test, it rained continuously for four days. This test was conducted immediately after the rain stopped. On the day of the test, the rain turned to sunshine, and there was a light wind of force 2. The procedure was the same as that in the previous experiment. Although a low-temperature anomaly region was present in this test, the difference in temperature between the leakage port and the surrounding areas was not particularly obvious because of the rainfall. The temperature anomaly surface spread to both sides but did not form a trailing shape; rather, it formed a vein shape because of the residual rainwater on the slope.

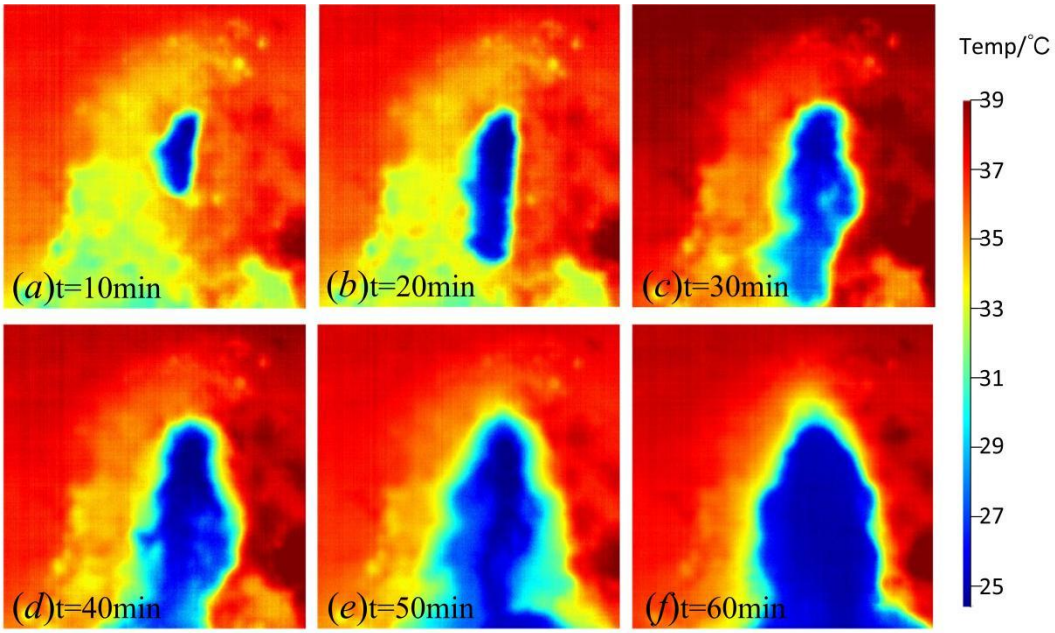


Fig.5. Leakage processes on slopes at midday on a sunny day

According to the above test results, the leakage process can be divided into four stages:

(1) Leakage formation stage: The internal structure of the embankment is damaged, creating a risk of pipe surge, but the temperature of the embankment surface is not affected, and there is no visible damage; thus, there are no abnormalities in the visible light or infrared images.

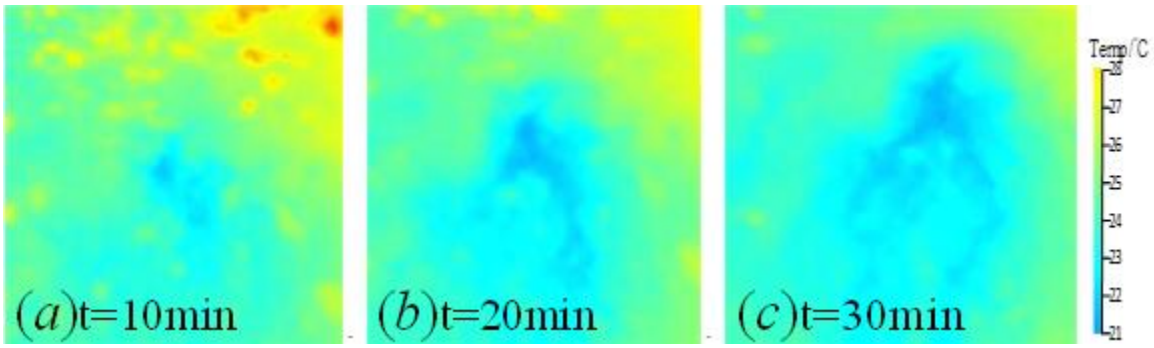


Fig.6. Afternoon leakage process on slopes after rain

(2) Slow leaching stage: A small amount of water infiltrates the embankment surface, forming a small area of low-temperature anomalies. At this time, the leakage point can be identified using infrared images, whereas detecting the anomaly using visible light or the naked eye is difficult.

(3) Leakage damage stage: The slope at the leakage point is damaged, and a large amount of water leaves the leakage point. The embankment surface shows more obvious signs of deformation and runoff. At this stage, visible light and infrared images can be used to detect the danger of leakage.

(4) Leakage stabilisation stage: After a long period of scouring, the deformation damage of the embankment surface becomes more stable, and the leakage path area stabilises.

In the last two tests, embankment leakage could be detected using infrared images after rainfall or on sunny afternoons. However, the low-temperature anomalies on sunny afternoons were greater than those after rainfall, making the infrared characteristics of embankment leakage more obvious and conducive to detection. Therefore, sunny afternoons may be the best time to detect embankment leakage during the flood season.

4.5 *Thermal imaging tests of concentrated seepage in turf-covered dam slopes*

In actual embankment projects, leakage points are usually covered by vegetation. To further investigate the feasibility of airborne infrared detection of earth and stone embankment leakage under vegetation influence, the previous test model was improved. As shown in Fig. 7, an additional leakage point was added to the original embankment surface to form a control group. To avoid interference between the two points, control leakage point A was set 50 cm from leakage point B. A 5-cm high turf was planted over a 30 cm × 30 cm area centered on point B.

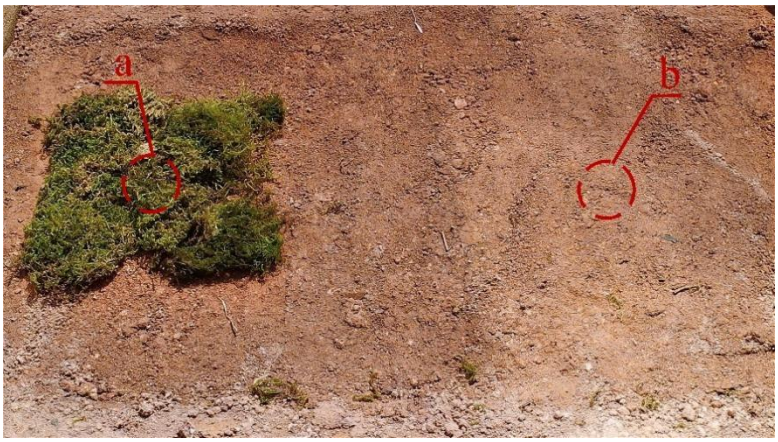


Fig.7. Turf-covered embankment model(*a*)Original leakage point(*b*) leakage point

Fig. 8 shows test results at noon on 24 June 2024, under sunny weather with a force 3 breeze. This experiment simulated more realistic conditions where seepage occurs through meadow. When the leakage inlet opened (t = 0), the dam surface and moss showed high temperatures due to direct sunlight. By t = 10 min, a low-temperature anomaly appeared at leakage point B, while point A remained unchanged. Around t = 20 min, point B formed a clear low-temperature zone with a trailing tail shape, whereas point A still showed no obvious change. By t = 30 min, seepage at point B had caused more stable slope damage and runoff, while point A eventually formed a low-temperature anomaly damaging the turf. The final low-temperature zones at both points were similar in size, but seepage rates differed significantly. Besides test errors, vegetation root systems can consolidate and regulate seepage, improve soil structure, and suppress piping development. In practice, suitable plants can be selected based on geological conditions and combined with engineering measures to form a synergistic protection system.

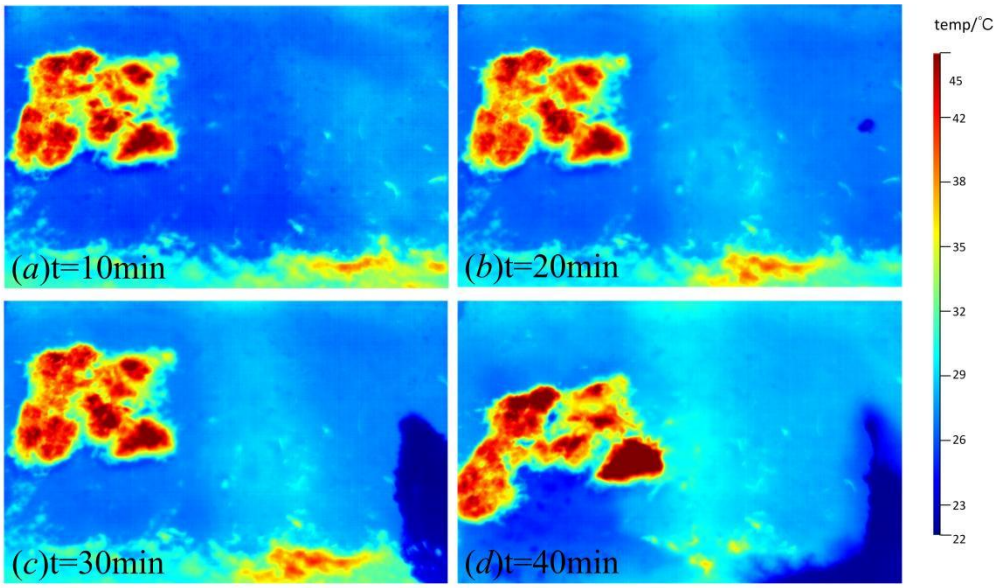


Fig.8. Turf covers the midday seepage process

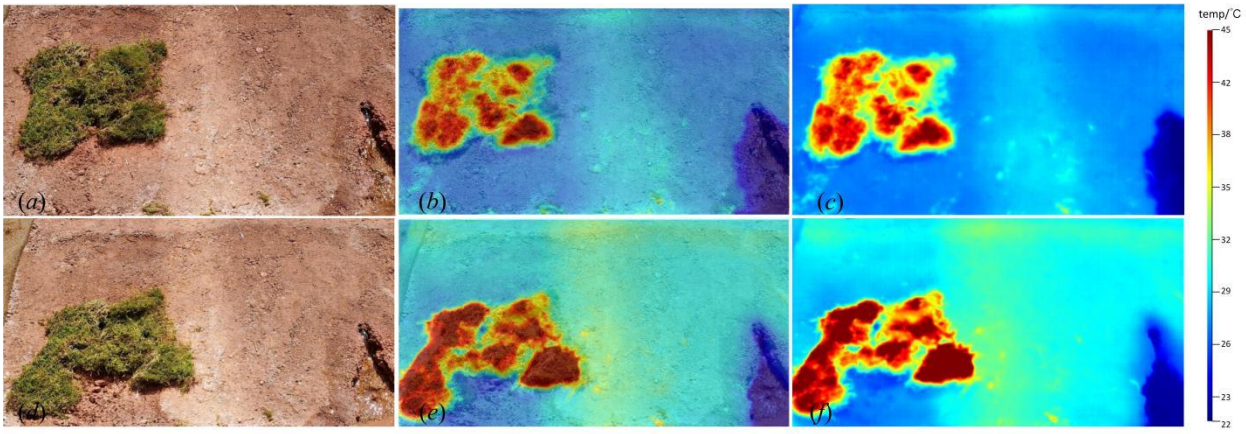


Fig.9. Image of turf covering midday seepage (*a*)No leakage visible (*b*)Leak-free fusion image (*c*)No i nfrared leakage (*d*)Visible light with leakage (*e*)Leakage Fusion Images (*f*)Infrared with leakage

The seepage process stages can be observed. In the slow leaching stage, small low-temperature anomalies form, undetectable by visible light or the naked eye. Compared to visible light, infrared images have lower resolution and lack spatial detail. Therefore, this study aligned infrared and visible images in the same coordinate system and fused them, as shown in Fig. 9. This allows quick identification of leakage characteristics via infrared, enhances visible image authenticity, and enables rapid localization of actual leaks in the levee.

5. ENGINEERING APPLICATIONS:

Previous laboratory experiments have verified the feasibility of using infrared thermal imaging to detect leaks in the slopes of earth–rock embankment dams under various natural environmental conditions. Low-temperature anomalies often occur in the late afternoon. In light of the dangerous pipe

surge situation (commonly known as “bubbling springs”) that occurred in the Triangle Lianxu area of Yongxiu County, Jiujiang city, Jiangxi Province, on 2 July 2024, a rapid inspection method based on an unmanned aircraft-mounted infrared camera for earth-rock embankment dams is being investigated, Expanding research into a fast method of inspecting dike leakage (Wang et al. 2023b).

As shown in Fig. 10, in this paper, a UAV-carried infrared camera was used to quickly scan the backwater of the embankment. Remote sensors control the UAV to obtain infrared and visible light images covering the full range of earth and stone embankments. This enables the noncontact detection of embankment hazards during the flood season.

5.1 *Project overview*

In 2024, water levels in the Yangtze River and Poyang Lake continued rising due to persistent heavy rainfall and upstream inflows. By 16:00 on 2 July, the water level at Xingzi Station on Poyang Lake reached 21.22 metres, exceeding the alert level by 2.22 metres, while Jiujiang Station on the Yangtze River recorded 21.56 metres, 1.56 metres above the alert level. At 12:00 on 2 July, Jiujiang city elevated its flood control emergency response to Level 2 and initiated Level 4 municipal disaster relief response.

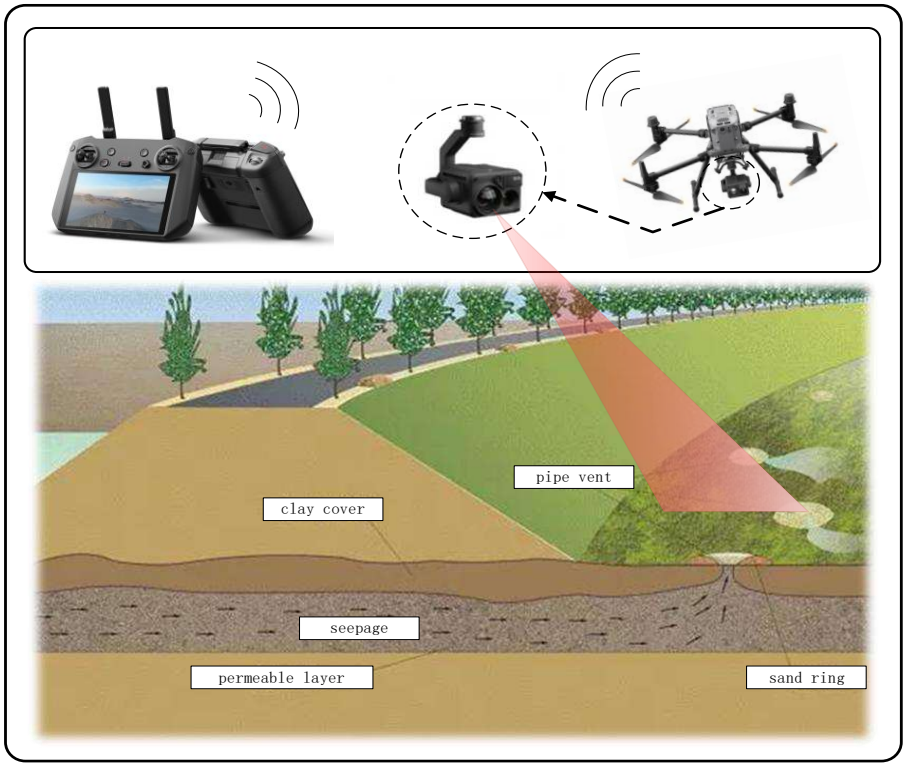


Fig.10. Schematic diagram of embankment inspection mode with airborne infrared camera

The rapid water level rise increased pressure on the dike, leading to continuous emergence of bubbling springs and seepage. On 29 June, two deep holes were detected on the outer slope (stakes 29+300 and 29+450) (Zhang et al. 2024). The same day, a bubbling spring was found at the dike foot (stake 29+200), followed by another on 2 July (stake 28+900), and another on 8 July (stake 29+1000). This paper focuses on the pipe surge

hazard identified on 2 July at Triangle Lianxu (stake 28+900), as shown in Fig. 11, aiming to support actual dike flood risk prevention and evaluate the practicality, feasibility and limitations of applying the previously discussed technology in engineering practice (Zhao et al. 2022a).

5.2 *Application process*

In this paper, a DJI Matrice 35 RTK UAV equipped with an H20T infrared thermal imaging sensor was used. This sensor can collect infrared and visible light images simultaneously within the same field of view. The main parameters of the onboard infrared and visible light detectors are shown in Tables 1 and 2, respectively.

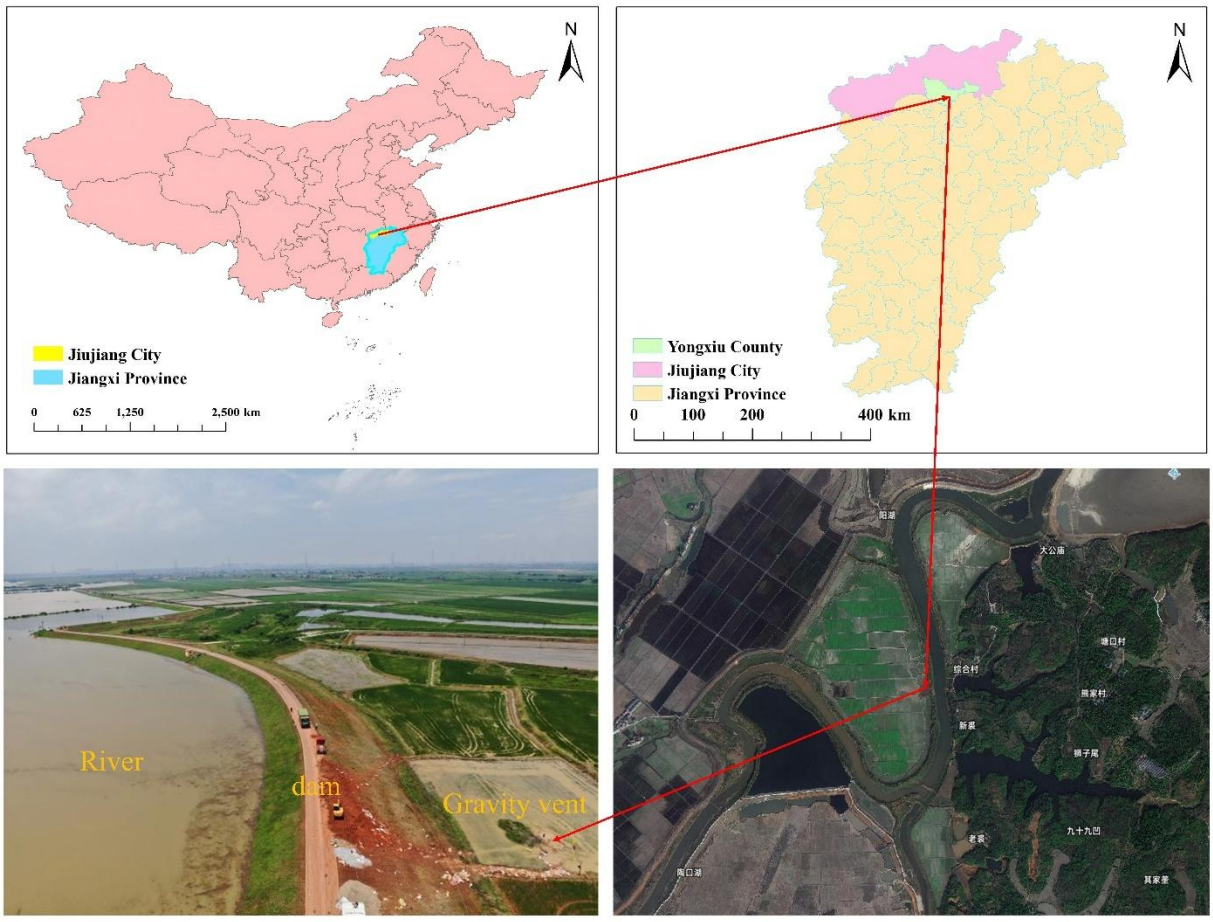


Fig.11. Geographic Location Map of Piping Risk at Triangular Joint Weir

The ground sampling distance (GSD) represents the actual size of a feature captured by a single pixel in an image. The relationships between the GSD (G) of a UAV image, the UAV altitude (H), the detector pixel size (δ) and the lens focal length (f) are given by the following equation:

(5)

When the imaging equipment is selected, the pixel size (δ) and lens focal length (f) are also determined. The feature resolution ability decreases as the height increases (G and H). Therefore, when the height of the

UAV is set to 25 m, the size of the detection target and the performance parameters of the dual-optical equipment should be considered.

5.3 *On-site inspection and verification*

The selected embankment is located in Yongxiu County, Jiujiang city, Jiangxi Province. The width of the top of the embankment was 5 m, its height was 1.5 m, and the slope ratios of the waterfront and backwater slopes were 1:2.5 and 1:3.0, respectively (Zhao et al. 2022b). The embankment was constructed on site using mainly powdery clay with miscellaneous fill distributed locally. Owing to river backflow, the embankment is subject to high water-level immersion, and seepage problems are prevalent, particularly at the foot of the embankment. During the flood season, there is a danger of slope seepage and tube surge. This inspection was conducted at midday on 2 July 2024, as shown in Fig. 12. The site of the inspection was located on the dike where pipe surge leakage occurred in the Lianxu Delta in Yongxiu County.

5.4 *Inspection results analysis*

An analysis of the image data obtained in this study revealed that it is broadly consistent with the test results obtained in the laboratory described in the previous section. Since the river's water body is larger and has a higher specific heat capacity than the soil material does, the temperature change rate of the water is lower than that of the soil under the same lighting conditions (Zhao et al. 2024). Therefore, the river temperature is lower than that of the slope surface on a sunny afternoon, resulting in the formation of a low-temperature anomalous area at the leakage outlet.Combining the previous test data with visible light and infrared images (Fig. 13) provides an intuitive representation of the temperature anomalies caused by seepage. Visible light increases the spatial realism of the leakage area, facilitating rapid spatial localisation and assisting in the identification of leakage.The engineering results show that using a UAV with visible light and infrared cameras to inspect embankments is feasible for detecting seepage. This method is simple to perform, highly efficient and intuitive, making it very practical for large-volume, long-line embankment projects. This is especially useful for areas that are difficult to access manually, such as pits, ponds, and paddy fields, as the method can be used to detect seepage and conduct a full investigation of embankment dams.

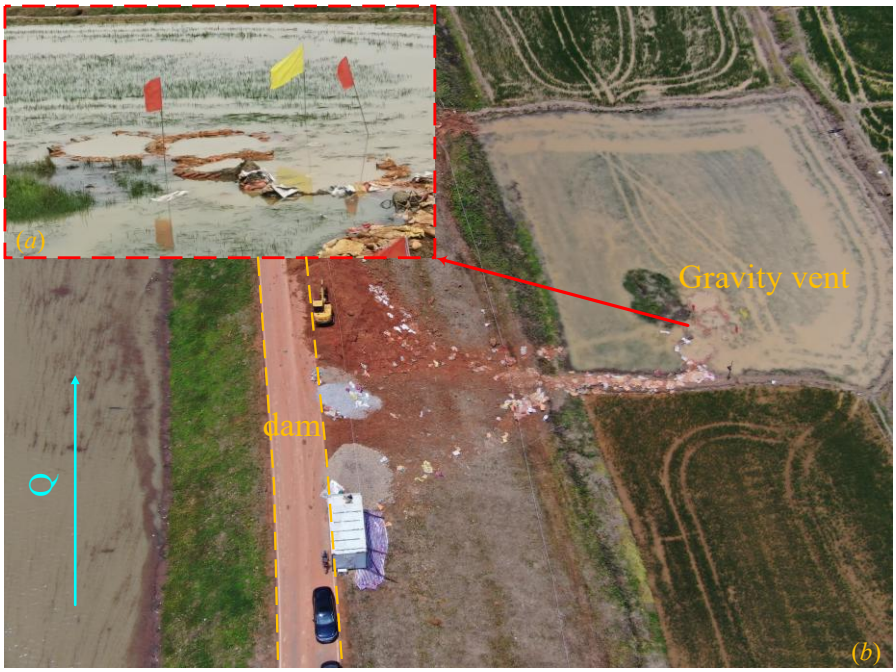


Fig.12. Pipe surge leakage at embankment sites(*a*) Localized view of the piping outlet(*b*) Leakage Overview

5.5 *Limitations of the inspection method in engineering applications*

Through laboratory testing and engineering inspections, as shown in Fig. 13, the practicality and feasibility of using an airborne infrared camera to detect seepage hazards in earthen embankments were confirmed. However, several limitations have been demonstrated.

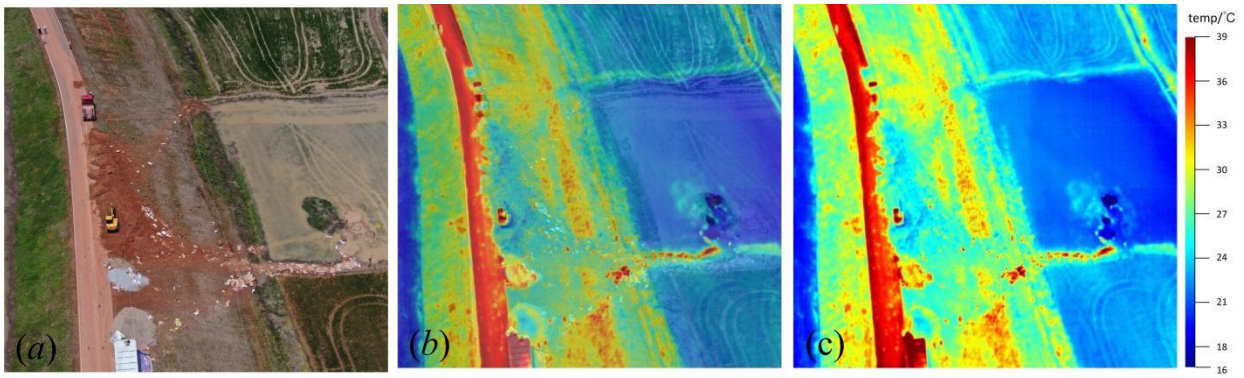


Fig.13. Images of levee site seepage (*a*)Visible light leakage (*b*) Seepage Fusion Image (*c*) Leakage Infrared Image

5.6 *Interference from complex weather conditions*

The core goal of airborne infrared seepage detection is to identify seepage points by capturing temperature anomalies caused by seepage. Therefore, the detection effect is highly dependent on the difference in temperature between the seepage outlet and the surrounding soil. As observed in the indoor experiments, the daily time window with an ideal temperature difference is limited (approximately 2–3

hours in the late afternoon). If this window is missed, the next ideal detection opportunity is on the following day, which may delay the emergency response to seepage hazards.

Weather conditions on the detection day also significantly affect the temperature difference: as shown in the postrainfall test, rainfall reduces the temperature difference between the seepage outlet and the surrounding soil, weakening the infrared signal of seepage and increasing the difficulty of detection. In addition, adverse weather conditions (e.g., strong winds, heavy rain, and heavy fog) can interfere with UAV flight and imaging quality:When the wind speed exceeds Level 4 (5.5–7.9 m/s), the UAV may experience unstable flight attitudes (e.g., yaw, roll), leading to deviations from the planned route and blurred images; in extreme cases, it may even cause loss of control.Rainwater can cause short circuits in the electrical system of a UAV, damage the camera lens, and form a water film on the embankment surface—this water film reduces the difference in temperature between the seepage outlet and the surrounding area, further interfering with infrared signal detection.Fog scatters infrared radiation, reducing the imaging resolution of the infrared camera and making it difficult to identify small-scale seepage anomalies.

Limitations in detecting internal seepage

By capturing the surface temperature anomalies of the embankment, the airborne infrared thermal imaging method can only identify seepage that has broken through the embankment surface (i.e., surface seepage). This method cannot detect internal seepage that has not yet broken through the surface (e.g., seepage channels formed in the middle layer of the embankment), as internal seepage does not cause obvious surface temperature changes. Therefore, this method is not suitable for early warning of internal seepage hazards and needs to be supplemented with other detection technologies (e.g., ground-penetrating radar and distributed fibre optics) to achieve comprehensive seepage monitoring.

5.7 ***Interference from surface coverings***

Although the results of the turf-covered slope test confirmed that infrared imaging can detect seepage through vegetation, dense vegetation or thick surface cover (e.g., straw, mulch) can weaken the infrared signal: the vegetation layer absorbs and scatters infrared radiation, reducing the temperature difference between the seepage outlet and the surrounding area and making identification of the “trailing” feature of seepage difficult. In addition, surface water accumulation (e.g., puddles formed by rainfall) can form false low-temperature anomaly areas, leading to misjudgement of seepage points.

6. CONCLUSION:

Through laboratory experiments and engineering applications, this study explored the feasibility of using UAV-mounted infrared cameras for rapid, noncontact detection of embankment seepage during flood seasons. By simulating different time periods and working conditions (uncovered slopes, turf-covered slopes, sunny days, and postrainfall), the infrared characteristics of embankment seepage

during flood seasons were clarified, and the practical application value of this technology was verified. The main conclusions are as follows:

(1) **Optimal Detection Time Window**: During sunny afternoons (12:00 p.m.–14:00 p.m.) and postrainfall periods, the difference in temperature between the river water and the embankment slope is relatively large, providing favourable conditions for infrared seepage detection. However, rainfall slightly reduces the slope temperature and weakens the temperature difference between the seepage outlet and the surrounding area. Therefore, sunny afternoons were determined to be the optimal time window for detecting seepage hazards in earth-rock embankments using airborne infrared cameras.

(2) **Infrared Characteristics of Seepage Points**: Under different environmental conditions, two typical infrared characteristics of seepage points were identified: *a.* **Trailing Feature**: Observed on sunny afternoons on uncovered slopes, the low-temperature anomaly area takes the seepage outlet as the centre and exhibits downwards gradient diffusion, forming a distinct trailing contour—this is the key identifier for seepage detection; *b*. **Vein-Like Feature**: Observed in postrainfall or turf-covered slopes, the low-temperature anomaly area spreads to both sides because of residual moisture or vegetation interference, forming a vein-like shape. These two characteristics can be used to identify seepage points in engineering applications, including vegetation-covered seepage points.

(3) **Effect of Vegetation on Seepage Detection**: Turf coverage of the embankment slope delays the appearance of low-temperature anomaly signals (by approximately 10–15 minutes compared with that of uncovered slopes) but does not prevent infrared detection of seepage. The turf root system can solidify the soil, inhibit piping development, and reduce the seepage rate—this provides a reference for the ecological protection of embankments.

(4) **Advantages of Dual-Spectrum Image Fusion**: The fusion of visible light and infrared images combines the high-resolution spatial information of visible light images with the temperature anomaly identification capability of infrared images. This not only enables rapid identification of seepage points on the basis of infrared characteristics but also achieves precise localisation of seepage points using visible light images, which is crucial for emergency disposal during flood seasons.

Data availabliity statement:

All data, models, or code generated or used during the study are available from the corresponding author by request.

Funding:

The authors gratefully acknowledge the support of the National Natural Science Foundation of China (52269027, 52669026), the Natural Science Foundation of Jiangxi Province (20242BAB23046), the Natural Science Foundation of Chongqing City (CSTB2024NSCQ-MSX0802) and the Science and

Technology Project of Jiangxi Provincial Department of Water Resources (202426ZDKT31). Critical comments by the anonymous reviewers greatly improved the initial manuscript.

Ethics declarations

Ethical Approval

All authors approved the ethics.

Consent to Participate

All authors agree to participate.

Consent to Publish

All authors agree to publish.

Competing Interests

The anthors have no relevant financial or non-financial interests to disclose.

Contributions:

Fugang Xu: Conceptualization, Formal analysis, Funding acquisition; KeSong Zhang: Data curation, Methodology, Writing–original draft; Folin Li: Investigation, Software; BoWen Wei: Supervision; Dongyang Yuan: Conceptualization, Writing-Review and editing; Lingyu Ouyang: Investigation, Software.

REFERENCES:

Abdelsamei, E., A. Tímár, D. Sheishah, V. Blanka-Végi, A. Hegyi, B. Runa, O. Balogh, A. M. Ali, and G. Sipos. 2024. "Detection of seepage zones in artificial levees: A case study at the Körös River, Hungary." Open Geosci., 16 (1): 12. https://doi.org/10.1515/geo-2022-0744.

Chen, B. L., Q. T. Duan, L. H. Luo, and W. Li. 2024. "Real-time levee seepage detection using UAV-borne thermal infrared imaging and edge computing-based YOLOv5." Int. J. Disaster Risk Reduct., 104: 104982. https://doi.org/10.1016/j.ijdrr.2024.104982.

Chen, S., Q. Zhong, and G. Shen. 2022. "Numerical modeling of earthen dam breach due to piping failure and validation by field detection." Comput. Geotech., 151: 104987. https://doi.org/10.1016/j.compgeo.2022.104987.

Duan, Q. T., B. L. Chen, and L. H. Luo. 2024. "Eigen-CAM-based visualization for interpreting deep learning models in levee seepage detection." IEEE Geosci. Remote Sens. Lett., 21: 1–5. https://doi.org/10.1109/LGRS.2024.3387654.

Ghimire, S. N., and J. W. Schulenberg. 2021. "An automated screening technique to identify at-risk auxiliary spillways: Modified approach in WinDAM." J. Hydraul. Eng., 147 (8): 04021045. https://doi.org/10.1061/(asce)hy.1943-7900.0001889.

Hu, Y. X., Q. Y. Jiang, and J. Pei. 2024. "Research on intelligent dam leakage detection technology using quasi-flow field method." Prog. Geophys., 39 (2): 781–787. https://doi.org/10.6038/pg2024HH0213.

Huang, Y., H. Qiu, and W. Gwenzi. 2022. "Validation of tracer test methods for quantifying dam leakage: A case study of a roller-compacted concrete dam." Water Resour. Res., 58 (9): e2022WR032189. https://doi.org/10.1029/2022WR032189.

Li, C. Z., G. Y. Liu, S. B. Xing, and J. Wang. 2025. "GPR data processing for levee hazard detection: Terrain correction and 3D imaging." J. Appl. Geophys., 232: 105489. https://doi.org/10.1016/j.jappgeo.2024.105489.

Liu, J., S. Zhang, and L. Tang. 2020. "Emergency detection of submerged seepage pathways in dams using acoustic emission technology." Ultrasonics, 107: 106289. https://doi.org/10.1016/j.ultras.2020.106289.

Liu, M., C. Wang, and H. Zhang. 2023a. "Lightweight YOLOv8-based real-time seepage detection for levees using thermal infrared images." IEEE Trans. Geosci. Remote Sens., 61: 1–12. https://doi.org/10.1109/TGRS.2023.3324567.

Liu, Y., H. Zhang, and C. Wang. 2023b. "Mask R-CNN-based precise segmentation of embankment piping areas in thermal infrared images." Comput. Electron. Agric., 208: 107658. https://doi.org/10.1016/j.compag.2023.107658.

Özer, I. E., S. Rikkert, F. Van Leijen, and J. K. Vrijling. 2024. "Sub-seasonal levee deformation observed using satellite radar interferometry to enhance flood protection." Sci. Rep., 14 (1): 18729. https://doi.org/10.1038/s41598-024-62156-x.

Senarathna, N. D. E. H. A., T. Dezert, and F. G. Sigtryggsdóttir. 2024. "Particle image velocimetry analysis of the protective layer in embankment dams." Front. Built Environ., 10: 1502168. https://doi.org/10.3389/fbuil.2024.1502168.

Su, H. Z., R. L. Zhou, M. K. Liu, and G. Chen. 2022. "Experimental study on seepage detection in earth-rock dams using passive infrared thermal imaging." Acta Hydraul. Sin. (Engl. Ser.), 53 (1): 54–67. https://doi.org/10.1061/(ASCE)HY.1943-7900.0002001.

552 Thomas, J., R. Klida, T. Oommen, and C. Miller. 2024. "Need for a multi-sensor monitoring approach for
553 embankment failures: Lessons learned from the Edenville dam failure." Environ. Eng. Geosci., 30
554 (1-2): 19–30. https://doi.org/10.21663/eeg-d-23-00056.

555 Tong, Y., F. Teng, and J. Lin. 2024. "Detection method and instrument design for piping paths in
556 earth-rock dams based on electric dipole sources." Chin. J. Geophys., 67 (12): 4522–4534.
557 https://doi.org/10.6038/cjg2024S0117.

558 Wang, H., S. Liu, and J. Zhang. 2023a. "Field investigation of dam leakage using distributed fiber optic
559 sensing (DFOS) technology." Water Resour. Res., 59 (8): e2022WR033456.
560 https://doi.org/10.1029/2022WR033456.

561 Wang, J., Y. Li, and L. Zhang. 2023b. "UAV-borne dual-spectrum imaging (infrared + visible) for
562 real-time levee hazard detection in complex terrain." Remote Sens., 15 (8): 2056.
563 https://doi.org/10.3390/rs15082056.

564 Zhang, Y., W. Li, B. Chen, and X. Zhao. 2024. "Multi-level hazard detection using a UAV-mounted
565 multi-sensor for levee inspection." Drones, 8 (3): 90. https://doi.org/10.3390/drones8030090.

566 Zhao, W., X. Chen, and Z. Li. 2022a. "Multi-source data fusion for levee seepage risk assessment during
567 flood season: Integrating infrared thermography, piezometer and rainfall data." Hydrol. Process.,
568 36 (12): e14932. https://doi.org/10.1002/hyp.14712.

569 Zhao, W., X. Chen, and Z. Li. 2022b. "Risk assessment of embankment seepage during flood season
570 based on multi-source detection data." J. Hydraul. Eng., 148 (6): 04022035.
571 https://doi.org/10.1061/(ASCE)HY.1943-7900.0002018.

572 Zhao, X., H. Zhang, P. Wang, and J. Liu. 2024. "Improving efficiency and accuracy of levee hazard
573 detection with deep learning." Comput. Geosci., 187: 105593.
574 https://doi.org/10.1016/j.cageo.2024.105593.

TABLES:

Table 1 Physical Parameters of the Experimental Embankment Soil

Table 2 Technical Parameters of the DJI Zenmuse H20T Infrared Camera

Table 3 Technical Parameters of the DJI Matrice 35 RTK UAV

FIGURE CAPTION LIST:

Fig. 1. Optical spectral region and energy jump correlation map

Fig.2. Arrangement of the test model platform: (*a*) top view (*b*) left view (*c*) front view (*d*) dimensions of the test dam

Fig.3. Time-varying process lines of environmental quantities in the test site area

Fig. 4. Thermal images of leakage outlets and their binarized segmentation results(*a*)Leakage thermal image(*b*)Leakage extraction results

Fig.5. Leakage processes on slopes at midday on a sunny day

Fig.6. Afternoon leakage process on slopes after rain

Fig.7. Turf-covered embankment model(*a*)Original leakage point(*b*) leakage point

Fig.8. Turf covers the midday seepage process

Fig.9. Image of turf covering midday seepage (*a*)No leakage visible (*b*)Leak-free fusion image (*c*) No infrared leakage (*d*)Visible light with leakage (*e*)Leakage Fusion Images (*f*)Infrared with leaka ge

Fig.10. Schematic diagram of embankment inspection mode with airborne infrared camera

Fig.11. Geographic Location Map of Piping Risk at Triangular Joint Weir

Fig.12. Pipe surge leakage at embankment sites(*a*) Localized view of the piping outlet(*b*) Leakage Overview

Fig.13. Images of levee site seepage (*a*)Visible light leakage (*b*) Seepage Fusion Image (*c*) Leakage Infrared Image